STUDY OF IMPULSE FORCING ON A SIMPLY SUPPORTED BLADE

By

TRINA SUE KRAUSSE

Bachelor of Science

Oklahoma State University

Stillwater, Oklahoma

2002

Submitted to the faculty of the Graduate College of
Oklahoma State University in partial fulfillment
of the requirements for the Degree of
MASTERS OF SCIENCE
May, 2005.

STUDY OF IMPULSE FORCING ON A SIMPLY

SUPPORTED BLADE

Thesis approved:

__Andy Arena_____
Thesis Advisor

___Peter Moretti_____

___Frank Chambers_____

____A. Gordon Emslie_____
Dean of the Graduate College

Acknowledgements

This research was in part supported by Universal Technology Corporation, Prime Contract F33615-02-D-2299, Delivery Order 0022, Subcontract Agreement 03-S530-0022-02-C1. Ms. Michele Puterbaugh acted as Program Manager for Universal Technology Corporation. Dr. Charles Cross, Air Force Research Laboratories, Propulsion Directorate, acted as Air Force Program Manager.

Table of Contents

Acknowledgements iii

Table of Contents iv

List of Tables vi

List of Figures vii

List of Nomenclature ix

1 Introduction and Background 1

2 Literature Review 5

2.1 Previous Experiments 5

2.2 Flow Behind a Cylinder 9

3 Experimental Set-up 10

3.1 Equipment 10

3.2 Scope of Testing 16

4 Hot-Wire Anemometer Measurements 19

4.1 Frequencies 19

4.2 Measured Velocities 22

5 Strain Measurements 24

5.1 No Mechanical Forcing 24

5.2 Sinusoidal Forcing 29

5.3 Impulse Forcing 32

5.4 Sinusoidal and Impulse Forcing 34

5.4.1 Variable-Frequency Multiple Impulses 34
5.4.2 Variable-Amplitude Multiple Impulses 36
5.4.3 Random-Amplitude Constant-Frequency Impulses 38
5.4.4 Combined Sinusoidal/Impulse Forcing 40
6 Conclusions 43

References 46

A.1 Uncertainty of the Anemometer Velocity 48

A.2 Strain Uncertainty 50

A.3 Displacement Uncertainty 53

List of Tables

Table 3-1 Aerodynamic Forcing Frequency Dependence on V_∞ and D 17

Table 4-1 Comparison of Predicted and Measured Frequency 21

Table 4-2 Velocity Mean and Standard Deviation without the Blade 22

Table 4-3 Velocity Mean and Standard Deviation with the Blade 22

Table A-1 Variables and Defined Values 51

List of Figures

Figure 3.1 Oklahoma State University Low-Speed Wind Tunnel Facility..... 11

Figure 3.2 Sketch of Equipment Layout..... 12

Figure 3.3 Sketch of Blade-Cylinder-Hot-wire Layout..... 14

Figure 4.1 Frequency Response No Forcing: a) Blade b) No Blade 20

Figure 4.2 Frequency Response 2.376-in: a) Blade b) No Blade 20

Figure 4.3 Frequency Response No Blade: a) 3.50-in b) 4.50-in 21

Figure 5.1. Blade Strain: No Mechanical Forcing, Variable D, V_∞ =53 ft/s 25

Figure 5.2. Blade Strain: No Mechanical Forcing, Variable V_∞, D=3.50-in. 26

Figure 5.3. Strain Probability: No Mechanical Forcing, V_∞ = 53 ft/s. 28

Figure 5.4. Strain Probability: No Mechanical Forcing, D = 3.50-in. 28

Figure 5.5. Strain Probability: Sinusoidal Forcing, V_∞ = 53 ft/s. 30

Figure 5.6. Strain Probability: Sinusoidal Forcing, D = 3.50-in. 30

Figure 5.7. Strain Probability: Single Impulse Forcing, V_∞ = 53 ft/s. 33

Figure 5.8. Strain Probability: Single Impulse Forcing, D = 3.50-in. 34

Figure 5.9. Blade Strain: Variable-Frequency Mechanical Impulse, No Cylinders, V_∞ = 53 ft/s. 35

Figure 5.10. Strain Probability: Variable-Frequency Mechanical Impulse, No Cylinders, V_∞ = 53 ft/s. 36

Figure 5.11. Blade Strain: Variable-Amplitude Mechanical Impulse, No Cylinders, V_∞ = 53 ft/s. 37

Figure 5.12. Strain Probability: Variable-Amplitude Mechanical Impulse, No Cylinders, V_∞ = 53 ft/s. 37

Figure 5.13. Blade Strain: Constant-Frequency Random-Amplitude Mechanical Impulse, V_∞ = 53 ft/s. 39

Figure 5.14. Strain Probability: Multiple Random-Amplitude Mechanical Impulse, V_∞ = 53 ft/s. 40

Figure 5.15. Strain Probability: Multiple Random-Amplitude Mechanical Impulse, D = 3.50 in. 40

Figure 5.16. Strain Probability: Combined Sinusoidal/Impulse Forcing, V_∞ = 53 ft/s. ... 41

Figure 5.17. Strain Probability: Combined Sinusoidal/Impulse Forcing, D = 3.50 in. 42

List of Nomenclature

Symbols

C	Blade chord
D	Diameter of cylinders
f	Frequency
k	Reduced frequency
St	Strouhal number
V	Voltage
V_∞	Freestream Velocity
ε	Strain

Acronyms

HFC	High Cycle Fatigue
NI	National Instruments

1 Introduction and Background

This section focuses on previous and current research on the topic of aerodynamic damping of rotor blades and the motivation for this research.

Turbine-engine high cycle fatigue (HCF) failures are often attributed to time-dependent fluid-structure interactions inherent to compressor/turbine blade row operation. In general, rotational motion between blade rows produces an unsteady aerodynamic environment composed of propagating flow disturbances (e.g., convective wakes) having harmonic frequencies related to shaft rotational speed and blade count. Interaction between such disturbances and neighboring blade rows causes unsteady aerodynamic blade loading, resulting in blade forced response (vibrations) and time-alternating blade strain. Unabated, blade forced response and strain causes blade fatigue damage accumulation, leading to possible crack initiation and catastrophic blade failure. Design methodologies established to mitigate turbine-engine HCF rely largely on experimentally determined material endurance limits. Endurance limits define the maximum alternating stress/strain levels to which a blade may be subjected to without possibility of fatigue failure. Despite the use of endurance limits, however, HCF-related blade failures continue to occur, suggesting endurance-based fatigue predictions to be inadequate. Such inadequacies may, in part, be attributed to inaccurate blade strain and/or aerodynamic forcing predictions. The current paper proposes blade strain and aerodynamic forcing predictions to be inaccurate due to improper modeling of random

blade-strain amplifications, such as those that might be induced by ingested inlet distortions.

Random strain amplifications are not modeled during endurance-limit development; endurance limits are typically based on constant-amplitude sinusoidal stress/strain histories. Given that such events may significantly accelerate blade fatigue damage accumulation, endurance-based designs may never achieve the reliability required for fail-safe engine operation. To be effective, endurance limits may require a probabilistic definition, allowing blade HCF failure predictions to be based on levels of confidence; e.g., fail-safe operation insured with 95% confidence. Probabilistic endurance-limit definitions would, however, require consideration of several factors to allow the accurate determination of confidence levels. For instance, an accurate accounting of probabilistically distributed microscopic material defects (stress concentrations), aerodynamic forcing-function variability, and aperiodic blade resonance events would be required. Previous investigations, such as those of Whaley[1-4] and Sanders and Fleeter[5], have examined the influences of probabilistically distributed material defects and aerodynamic forcing functions on turbine-engine HCF, respectively. The current paper focuses on the influence of aperiodic blade-resonance "events" on blade forced response; particularly in terms of strain amplification and probability distribution.

At its most basic level, turbine-engine compressor/turbine blade forced response has been traditionally predicted via Campbell diagrams. Campbell diagrams describe the engine conditions under which known periodic aerodynamic excitations coincide with the known structural natural frequencies of a blade row, indicating possible blade resonance.

Using a Campbell diagram, the likelihood of inducing a blade-resonance event via periodic forcing can be tracked by monitoring blade rotational speed. Campbell diagrams do not, however, account for blade resonance induced by non-periodic excitations (i.e., independent of shaft speed). Non-periodic excitation sources include phenomena such as inlet distortions, foreign object damage/impact (FOD), and aerodynamic variability, all of which could have sufficient energy and duration to overcome blade inertia, excite oscillatory motion, and amplify blade strain. Due to their arbitrary nature, the occurrence of such non-periodic blade-resonance "events" may be distributed over the operational life of an engine, with each event leading to possibility significant blade-strain amplification. Therefore, with the occurrence of each blade-resonance event, blade fatigue damage accumulation may be accelerated, while the applicability of traditional material endurance limits and Campbell diagrams is reduced.

Provided this interpretation of blade forced response, it is argued that accurate turbine-engine HCF models must be probabilistically based, assessing fatigue failure on the occurrence of blade-resonance events, not the number of engine/forcing cycles. For instance, assuming the blade aerodynamic forcing environment is well characterized and aperiodic blade-resonance events do not occur, blade alternating strain levels should never exceed the design endurance limit, regardless of the number of forcing cycles. Conversely, if a significant number of blade-resonance events do occur during several forcing cycles, blade alternating strain levels may amplify above the design endurance limit, accelerating material fatigue damage in a non-deterministic manner. In this case, the use of endurance limits, or even forcing-cycle counting, would lead to inaccurate HCF predictions.

The goal of the current paper is to examine blade strain variability under both mechanical and aerodynamic forcing, where the forcing is both periodic (sinusoidal) and aperiodic (impulse). Results from this paper are intended to establish an initial link between the occurrence of random blade-strain amplification events and blade fatigue life. Since this investigation is the first of its kind, an elementary approach is undertaken, with all experiments conducted in a low-speed wind tunnel on a non-rotating simply supported blade. Time-dependent blade strain measurements are presented, showing blade-strain probability distribution dependence on forcing and mean aerodynamic conditions.

2 Literature Review

This chapter will focus on experiments previously performed related to failure of turbomachinery and understanding what is causing the frequency responses. Also included is the theory of cylinder wakes.

2.1 Previous Experiments

Many different experiments have been conducted to investigate different aspects of the forcing conditions in turbomachinery. Some are very simple and only use a single blade while others try to be more inclusive and use complete engines. The main focus of all the experiments is trying to determine what the contributing forces are and from where they come.

The same basic experimental procedure was followed in all the experiments. Crawley[17] laid out the basic steps the best. They are as follows:

1. Develop the equations of motion of the blade disk system, which adequately characterize the modes expected in the aeroelastic response. Experimentally verify the modal frequencies, shapes, and structural damping.
2. Instrument the rotor to gain sufficient data to identify the modal responses.
3. Run the aeroelastic experiment collecting data on every blade response and disk participation and analyze the data in the following manner:

a. Identify by Fourier transformation in time, the dominate frequencies of response, and the blade modes (first bending, etc.) with which they are associated.
b. Narrow band pass filter the raw data to isolate each frequency of response.
c. Use the modal relations and measured displacements to transform to multiblade coordinates. [3]

The earliest experiment looked at was conducted by E. F. Crawley[17] using the MIT Transonic Compressor run in the MIT Blowdown Compressor Test Facility. He tried to isolate the effects of structural damping and aerodynamic damping. Crawley used strain gages and piezoelectric crystals to detect the motion of the blades with respect to the hub. The measurements are reduced using Fourier transforms to determine the modal frequencies. The amplitude of the oscillations for each blade was also recorded. Crawley's conclusion is that the final result is a direct measurement of the aerodynamic and structural damping, which are functions of the interblade phase angle and reduced frequency. He used a structural model to separate the structural damping from the aerodynamic damping instead of through experimental measures that others have used.

The next experiment looked at was conducted by Buffum and Fleeter[16] in the NASA Lewis Research Center Transonic Oscillating Cascade Facility. The data collected was the oscillatory response. Kulite surface mount pressure transducers measured the unsteady airfoil surface pressures along each side of a blade. The data was reduced using Fourier transforms. Two independent sensors determined the time-variant position of the oscillating airfoil. The two were an electro-optical displacement meter and a proximity probe sensor. It was determined they both gave similar results but that the proximity

probe was more reliable and less susceptible to measurement noise. The experiments investigated and quantified the effects of inlet Mach number, reduced frequency, interblade phase angle, and mean flow incident angle on the unsteady aerodynamics of the oscillating cascade.

Kenyon and Rabe[9] were interested in how mistuning in a blisk would contribute to high-cycle fatigue in an engine. The fatigue is mainly caused by stresses induced in the blisk. This is the physical parameter measured in this experiment. A blisk was studied because in the past more effort has been devoted to blade and hub assemblies and blisks are becoming more common in practical applications. A forcing function was produced with a mesh screen to excite the desired resonant condition. The forcing function was measured and quantified before the response of the blisk was determined. The blisk was then instrumented with strain gages to measure the oscillatory response during resonance.

It was found that for this blisk the structural mistuning was very low. The lack of correlation between natural frequency and mean peak stress indicate that variations in stress are influenced by factors other than blade mistuning. One possibility was hub modal participation. It was rule out due to the phase data and finite element modeling of the rotor did not support hub participation. Unsteady aerodynamic coupling is the second possible factor. It was not looked into in depth but it was noticed that a relationship between speed and blade-to-blade stress distribution existed. In blisk structural damping is very small in comparison to aerodynamic damping and is often neglected. Aerodynamic damping variations were shown to correspond roughly with blade-to-blade stress amplitude variations. Conclusion need to better understand the unsteady aerodynamic effects.

Frey and Fleeter[18] conducted the next study. Their experiments were conducted in a research compressor. The compressor was set up such that individual blades could be forced to see the effect that the motion of one blade had on the neighboring blades. The experiments were directed at investigating and quantifying the aerodynamic damping of the first stage rotor. In general the aerodynamic influence of the oscillating blade decays rapidly with increasing distance from the reference blade. The influence is different on the suction and pressure surfaces. May need to go beyond the first harmonic to analysis oscillating airfoil aerodynamics for flutter and forced response at high amplitudes of oscillation. It was also determined that the aerodynamic damping was not always linear in nature.

Kielb and Abhari[19] performed the final experiment investigated. The experiment was conducted at the Ohio State University Turbine Research Facility. They tried to make the experiment as real life like as possible. They instrumented six blades. Two blades were instrumented with strain gages only while the other four blades had strain gages and piezoelectric ceramic actuators. Once again Fourier transformations were used to reduce the data. This set up was decided on to try to see the effects of the instrumentation.

The experiment was conducted in a vacuum and in air. In the vacuum the only significant damping present came from friction between the blade and the disk attachment. This was used to isolate aerodynamic effects from structural effects on the damping. The structural damping was shown to be inversely proportional to the square of the speed. The effects of the aerodynamic damping were more significant than the

authors had thought when compared to the structural damping. The structural damping and aerodynamic damping were measured for different modes.

Srinivasan[20] conducted a survey of the advancements in the theoretical models and experiments concerning the vibrations of bladed-disk assemblies for the decade of 1973-1983. Through his survey he found many things that were important including structural and aerodynamic components. In general, he found that more work needed to be done to investigate the complexities of the system and to verify theoretical models through experiments. His survey is still very important and his conclusions still hold. Since his survey more work has been done. However most of the newer models still refer to the same limited set of experiments collected in 1983.

All the papers lead to the feeling that there is more to be done to understand what is happening in the system and to better quantify the causes of the oscillatory motion. As the models have been updated with improvements in understanding and computing power the need for more specific experiments has arisen.

2.2 Flow Behind a Cylinder

The flow behind a circular cylinder is a series of vortices shed alternately from each side of the cylinder. These shed vortices are referred to as Karman vortex sheets. The frequency of the vortex shedding is governed by the Strouhal number, which accounts for the diameter of the cylinder and the free stream velocity. The shedding cycle takes place during the first five cylinder diameters[21].

3 Experimental Set-up

The following chapter outlines the equipment used, the instrumentation and the types of information collected.

3.1 Equipment

All experiments were conducted in the Oklahoma State University (OSU) low-speed wind-tunnel (illustrated in Figure 3.1). This tunnel is an open-loop facility, being comprised of an 15:1 inlet contraction nozzle, constant-area test section, diffuser and blower. The 60.0 in-diameter radial-inflow blower is powered by a 125 hp variable speed electric motor, capable of pulling up to $1.0 \cdot 10^5$ cfm of air through the test section. The blower makes use of airfoil-shaped Acoustafoil blades, resulting in a stable pressure curve over the entire tunnel operating range, while also reducing structural vibrations, mean-flow unsteadiness and surging. Numerous flow management devices, such as honeycomb materials and high-density mesh screens, exist upstream of the inlet nozzle and forward of the blower. These devices reduce lateral and axial flow fluctuations and swirl. Tunnel flow quality is characterized by turbulence intensity values less than 0.10%.

The tunnel test section is 9.0 ft in length, with a 3.0 ft × 3.0 ft cross-sectional area, allowing maximum freestream velocities up to 185 ft/s and a Reynolds number per foot

capability of approximately 1.2×10^6. This large test-section cross-sectional area allows relatively low blockage without sacrificing flow quality; giving only 11.0% blockage per square foot of model frontal area. In the current experiment, one test-section wall was constructed of transparent Plexiglass, allowing for the use of a laser vibrometer to collect time-accurate blade displacement data. A ±10.0 inH_2O Meriam Instrument 350-DN0020 Smart Manometer Pressure gage allowed for freestream velocity measurements via standard pitot-static probes mounted downstream of the test blade.

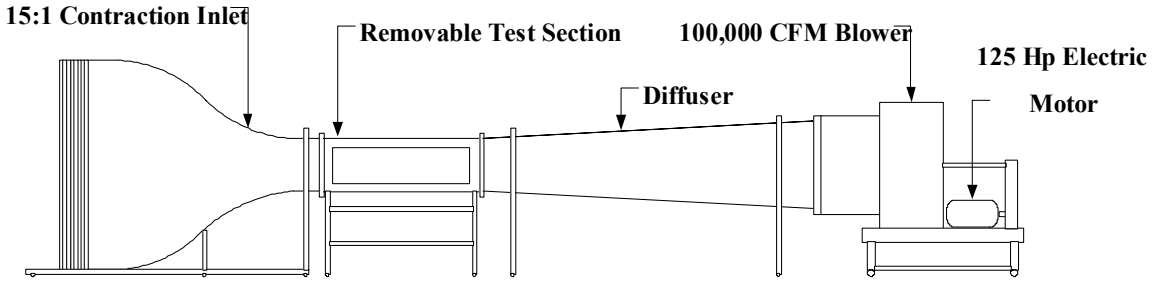

Figure 3.1 Oklahoma State University Low-Speed Wind Tunnel Facility.

The test blade consisted of simply supported, untwisted, rectangular flat plate operating at zero-mean incidence relative to the freestream. The blade experimental setup is illustrated in Figure 3.2. A flat-plate profile was selected to ease construction, reduce manufacturing time and expense, simplify blade response modes, and remove mean-loading. A 5.25-in blade chord was selected to closely mimic mean-flow conditions (i.e., Mach number and Reynolds number) experienced by the rotor in the OSU axial-flow research compressor; in preparation for future follow-on experiments. A long blade span was selected to minimize mode coupling[6] and increase tip deflection for a given electromechanical shaker input; however, this long span was also found to increase instrumentation difficulty, complicate blade construction, and exacerbate the

geometric differences between the test blade and OSU axial-flow research compressor rotor. Therefore, as a compromise, a 10.0-in blade span was selected, providing an aspect ratio of 1.90.

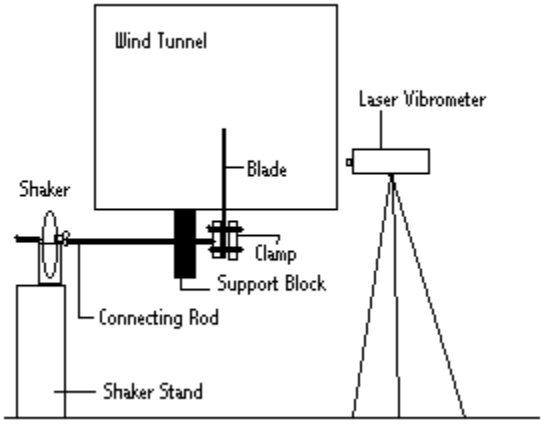

Figure 3.2 Sketch of Equipment Layout

Note that, in the described configuration, the blade-forcing experiments did not include the influences of blade rotation, neighboring blades, blade-row interactions, or mean aerodynamic loading, as found in an actual rotor. In fact, the experiments were purposely simplified to facilitate the isolation, control, and measurement of induced blade-resonance events. Such simplification was deemed necessary for this initial parametric investigation, providing a basis of comparison for future, more complicated, blade-forcing studies.

The blade was introduced into the wind tunnel through a narrow slot in the test-section floor, as shown in Figure 3.2. The slot size was minimized to three times the blade thickness, in an effort to reduce flow leakage. An aluminum clamping mechanism

supported the blade position within the tunnel, and also provided for a solid connection between the blade and a electromechanical shaker. In order to promote blade forcing of the first-bending mode, the shaker was placed exterior and to the side of the tunnel test section (see Figure 3.1). A rigid rod linked the shaker and blade clamping mechanism. The rod was supported by two linear bearings attached to a support system isolated from the walls of the tunnel. The linear bearings reduced misalignment between the shaker and clamping mechanism, eliminating unnecessary stress on the shaker head due to the blade weight. A rigid support stand was constructed to position the shaker at a height equal to that of the linear bearing, blade clamping mechanism, and test blade.

The 50-lb MB Dynamic PM-50A electromechanical shaker integrated with a Agilent 33220A 20MHz waveform generator, provides the capability to program sinusoidal, impulse, random, and combined sinusoidal/ impulse mechanical blade forcing of variable amplitude and frequency. In impulse mode, this forcing mechanism produced a single excitation of user-defined amplitude, exciting the blade into transient resonance. In random mode, mechanical forcing of random amplitude and periodicity was provided within user-defined bounds, exciting multiple arbitrary blade-resonance events in succession.

Aerodynamic forcing was provided by circular cylinders placed one blade-chord directly upstream of the blade. The cylinder shed wake vortices propagated downstream across the blade causing aerodynamic forcing. Aerodynamic forcing frequency was governed by the Strouhal number[21], as defined by Equation 1

$$St = \frac{fD}{V_\infty} = 0.2, \qquad \textbf{Equation 1}$$

where f represents the blade forcing frequency (i.e., wake shedding frequency, in Hz), D the cylinder diameter, and V_∞ the freestream velocity. Therefore, cylinder wake-shedding frequency was directly controlled by changes in cylinder diameter and freestream velocity. At the tested Reynolds numbers (i.e., $3.5 \times 10^4 - 2.3 \times 10^5$, based on cylinder diameter, D), the Strouhal number is known to be approximately constant at 0.2[7]. Three cylinders were chosen: 2.376-in, 3.50-in, and 4.50-in.

Cylinder wake effects were measured with a hot-wire anemometer. The anemometer system came from Dantec Dynamic. It consisted of the miniature Anemometer 54T30, probe support type 55H25 (straight), and a 2-D probe 55P11 special. The probe was positioned 1 inch upstream of the blade and mounted to allow vertical measurements from the bottom of the tunnel to the height of the blade as shown in Figure 3.3.

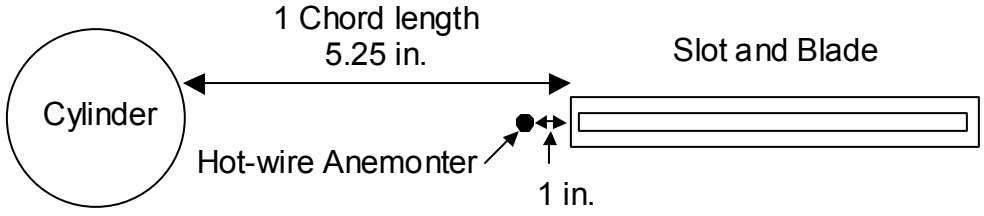

Figure 3.3 Sketch of Blade-Cylinder-Hot-wire Layout

A Dantec thermistor probe 55P32 was used with the anemometer to allow for temperature compensation. The thermistor is accurate to ± 0.3° (±0.54°F). The freestream velocity was measured using an Omega PX653-03D5V pressure transducer and an Omega PX 2760-800A5V barometer. All equipment was connected to an NI BNC-2090 breakout box. This data was collected via a high speed digital computer and

an NI digital acquisition system, including a PCI-66071E data acquisition card and accompanying LabView software version 6.1.

Both time-accurate blade strain and displacement measurements were collected. To measure blade strain, three Wheatstone bridges, each consisting of two Vishay Micro-Measurements Division CEA-13-250UW-350 precision strain gages, were placed at separate chordwise positions of 5, 44, and 95%c (where c is the blade chord) near the blade root, similar to the experiments of Manwaring et al.[8] and Kenyon et al.[9]. Finite-element modeling predicted maximum blade strain near the root for first-order bending oscillations. Each strain gauge was connected to a National Instruments SCXI-1520 signal conditioning amplifier, providing necessary bridge excitation, balancing, and output gain.

Blade displacement measurements were collected via a Polytec laser vibrometer system consisting of an OFV-350 sensor head and OFV-2600 vibrometer controller. The sensor head was positioned exterior to the tunnel test section on a three-axis tripod at a distance of approximately 10.5 in from the tunnel wall; the distance optimized to maximize vibrometer displacement sensitivity. As mounted, the vibrometer provided for displacement measurements at any blade chordwise or spanwise location visible through the transparent test-section sidewall. However, to increase sensitivity the vibrometer was vertically positioned to allow laser impingement near the blade tip, the location of maximum blade displacement.

All blade strain and displacement data were collected via a high-speed digital computer and sixteen-channel, National Instruments digital data acquisition system,

including a PCI-6024E data acquisition card and accompanying LabView software, version 6.1.

Uncertainty analysis for the anemometer, strain, and displacement data is shown in Appendix A. The uncertainty for the anemometer velocity data is ± 3.7%. The strain uncertainty is ± $2.628\times10^{-3}\mu\varepsilon$. This is a worst-case value. The uncertainty for the displacement is less than 3%. .The displacement results are not shown due to unresolved issues with voltage offset and drift within the results.

3.2 Scope of Testing

A series of experiments were conducted each to achieve a different piece of information. The testing was carried out in four stages: no mechanical or aerodynamic forcing, only mechanical forcing, only aerodynamic forcing, and a combined mechanical and aerodynamic forcing. The strain and displacement data were all collected in each of these four stages. The hot-wire data was only collected for no forcing and aerodynamic forcing.

The mechanical forcing can be divided into three main types: sinusoidal forcing, impulse forcing and a combined sinusoidal and impulse forcing. The sinusoidal forcing was chosen through preliminary calculations using Theodorsen's equation and the limitations of the shaker. The best sinusoidal forcing frequency was found to be 10 Hertz. The natural frequency of the blade is slightly less than 10 Hz but very close. After setting the 10 Hz starting point from the calculations numerous other frequencies were tried. The higher frequencies caused much smaller amplitudes and multiple nodes to form on the blade. Lowering the frequency was approaching the limits of the function generator and shaker. At 10 Hz the amplitude of the blade was great enough to detect

with both the strain gages and the laser vibrometer. Another factor affecting the amplitude of forcing was the size of the opening in the bottom of the tunnel. The smaller the opening the less air flow though the opening. The final opening was three times the width of the blade.

Impulse mechanical forcing was conducted via single impulse, multiple constant-amplitude impulse, multiple variable-amplitude impulse and multiple variable-frequency impulse types. Ten different amplitudes were chosen to represent the random unpredictable events that occur. Values chosen were both larger and smaller than the sinusoidal forcing. Using Agilent's random function generation program allowed inputs to be designed using each of the different amplitudes by itself, with any combination of the other amplitudes and at any frequency desired.

The aerodynamic forcing consisted of a convecting von Karman vortex sheet shed from an upstream cylinder, similar to the blade-forcing experiments of Fabian et al[10]. The cylinders were placed 1 chord length in front of the blade. To control the aerodynamic forcing, four free-stream velocities (30 ft/s, 53 ft/s, 76 ft/s and 100 ft/s) and three forcing-cylinder diameters (2.376-in, 3.50-in, and 4.50-in) were investigated. Table 3-1 indicates the approximate blade aerodynamic-forcing frequencies induced for each combination of free-stream velocities and cylinder diameter based on Equation 1, the Strouhal number.

Table 3-1 Aerodynamic Forcing Frequency Dependence on V_∞ and D

V∞	100 ft/s	76 ft/s	53 ft/s	30 ft/s
D = 2.376-in	101.0 Hz	76.8 Hz	53.5 Hz	30.3 Hz
D = 3.50-in	68.6 Hz	52.1 Hz	36.3 Hz	20.6 Hz
D = 4.50-in	53.3 Hz	40.5 Hz	28.3 Hz	16.0 Hz

For all the experiments 65536 sequential measurements were collected for each piece of data being collected. The strain measurements and displacement measurements were collected at a rate of 1000 Hz/input.

4 Hot-Wire Anemometer Measurements

This chapter focuses on the forcing produced by vortex sheet shedding from three different sized cylinders. A main concern was the frequency of the forcing provided by each cylinder at each velocity. The information will be looked at in two sections: the first dealing with the frequencies and the second with the measured velocities.

4.1 Frequencies

This section will focus on the frequencies produced by the cylinders and the effect of the blade on these frequencies. The values will be compared to the expected values, which will lead to the next section where the velocities will be discussed.

The following sets of figures show the frequency response of the anemometer readings. The first set is of the base frequency measured when no forcing is present with and with out the blade being present. The second set is the frequency response to the 2.376-in cylinder with and without the blade and the last set is the 3.50-in and 4.50-in cylinders without the blade. All of the results have been shifted for ease in reading. All original data was centered on zero. The scale of the amplitude is the same for all of the frequency responses in this chapter.

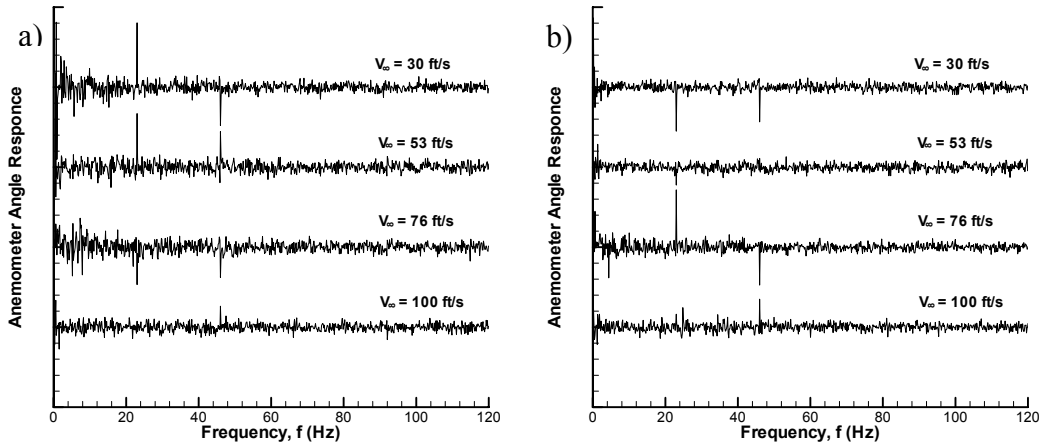

Figure 4.1 Frequency Response No Forcing: a) Blade b) No Blade

Figure 4.1 shows how the presence of the blade changes the frequency response seen by the hot-wire without any aerodynamic forcing. The largest change is that more frequencies are excited to a greater degree. Figure 4.1 is zoomed in by a factor of 100 when compared to the other figures in this chapter.

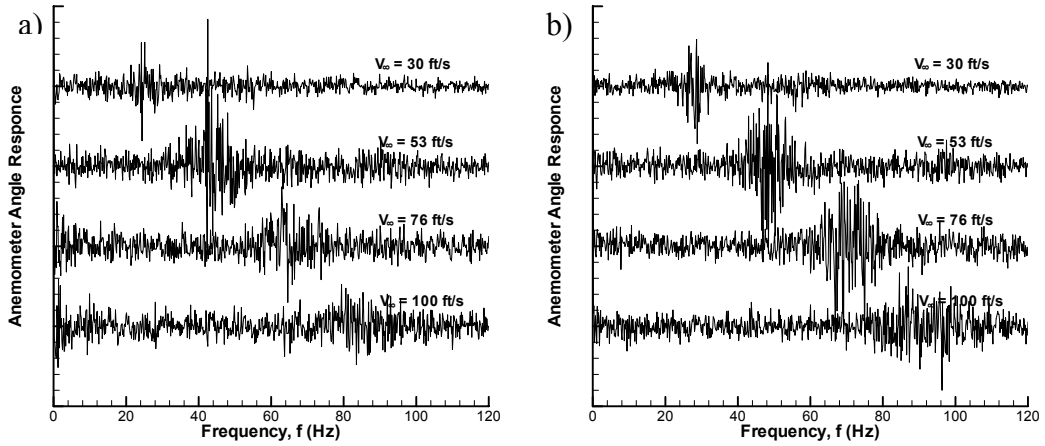

Figure 4.2 Frequency Response 2.376-in: a) Blade b) No Blade

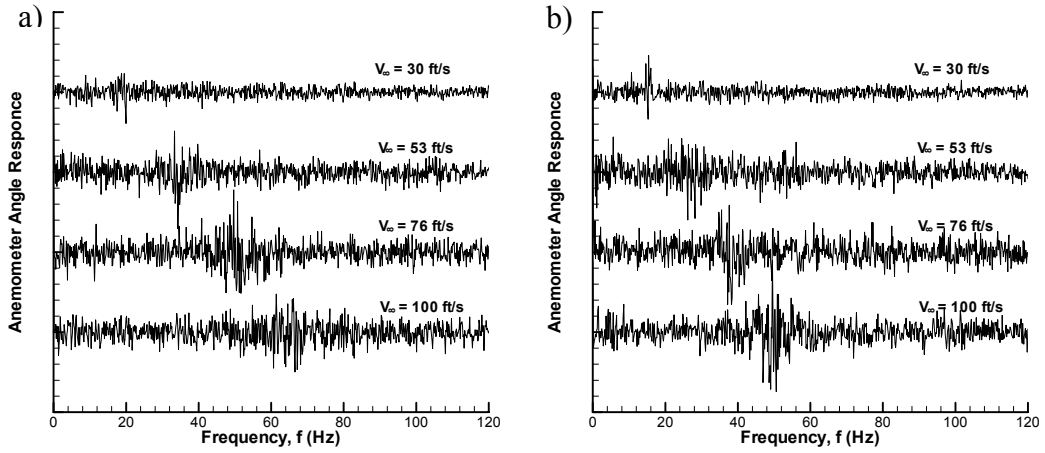

Figure 4.3 Frequency Response No Blade: a) 3.50-in b) 4.50-in

Introducing the blade had the greatest effect on the frequency of the 2.376-in cylinder. The frequencies for all velocities reduced by approximately 5 Hz. This is shown in Figure 4.2. However, for the other two cylinders the introduction of the blade only reduced the prominence of a main frequency and is not shown. Chapter 5 will detail the differences between the frequencies measured by the anemometer and the frequencies from the strain data collected.

The following table shows the calculated frequency using the Strouhal number and the frequency read from the figures. For all cases the measured frequency is lower than the calculated frequency. A contributing factor to the frequency mismatch is the slight variations from the ideal velocity in the freestream velocity measured.

Table 4-1 Comparison of Predicted and Measured Frequency

Frequency (Hz)	V∞ (ft/s)	D = 2.376-in	D = 3.50-in	D = 4.50-in
Measured		87	65	50
Predicted	100	101.0	68.6	53.3
% Diff		13.87	5.25	6.19
Measured		70	50	37
Predicted	76	76.77	52.1	40.5

% Diff		8.82	4.03	8.64
Measured		48	34	26
Predicted	53	53.54	36.3	28.3
% Diff		10.34	6.34	8.13
Measured		28	19	15
Predicted	30	30.30	20.6	16
% Diff		7.6	7.77	6.25

4.2 Measured Velocities

This section focuses on the velocities measured by the anemometer. The measured data was collected in coordinates at a 45-degree angle to the mean flow of the tunnel. The velocities were then rotated into the tunnel coordinates. The mean and the standard deviation of the velocities are shown in Table 4-2.

Table 4-2 Velocity Mean and Standard Deviation without the Blade

Units (ft/s)	No Cylinder		D = 2.376-in		D = 3.50-in		D = 4.50-in	
Freestream Velocity	Mean	Standard Deviation	Mean	Standard Deviation	Mean	Standard Deviation	Mean	Standard Deviation
30	30.16368	0.177458	28.44979	3.614129	28.56691	4.171537	28.13352	4.203033
53	50.8442	0.223111	38.65963	9.387025	35.97036	10.39981	36.47462	10.87027
76	74.42265	0.293507	49.56403	14.96865	47.4302	16.71928	49.29664	18.01192
100	97.93418	0.335659	60.90116	19.98827	61.28797	22.84815	59.56194	22.73102

Table 4-3 Velocity Mean and Standard Deviation with the Blade

Blade	No Cylinder		D = 2.376-in		D = 3.50-in		D = 4.50-in	
Freestream Velocity (ft/s)	Mean	Standard Deviation	Mean	Standard Deviation	Mean	Standard Deviation	Mean	Standard Deviation
30	30.43828	0.123676	28.00589	3.546873	28.70831	5.202693	29.97962	5.869679
53	50.12242	0.193085	37.24627	9.11439	27.94914	3.84477	27.19718	3.330012
76	74.06997	0.303904	42.32166	13.35482	34.53403	7.788619	36.12817	9.181319
100	97.31706	0.351669	53.22245	18.23567	45.52438	12.91749	46.81144	13.95554

By comparing the freestream velocities and the mean velocity in the wake of the cylinder it can be seen that the mean velocity seen by the probe is less than the freestream velocity. A small part of this can be accounted for by the uncertainty in the measurements. The anemometer corresponds very well with the pitot-static tube when there is no aerodynamic forcing. This proves that the calibration was good. Another possible reason for the difference in the velocity could be due to the turbulence in the wake of the cylinder.

5 Strain Measurements

This chapter will look at the frequency and strain response of the blade to the mechanical and aerodynamic forcing. Also, the reasoning behind not taking into account some of the possible forcing conditions will be addressed. The chapter will be divided according the different mechanical forcing applied.

5.1 No Mechanical Forcing

The first case investigated was how the blade reacted just to changes in the airflow. In this case, the blade was allowed to respond freely to aerodynamic forcing from the freestream and forcing cylinders. Four different aerodynamic forcing cases were looked at: no upstream disturbance, and an upstream disturbance caused by a 2.376-in, 3.50-in and a 4.50-in cylinder. The overall behavior of the three different cylinders was very similar so that only the no mechanical forcing and the 3.50-in cylinder will be discussed in detail. Both the 2.376-in and 4.50-in cylinders followed the same patterns however the 2.376-in was less pronounced and the 4.50-in was more pronounced.

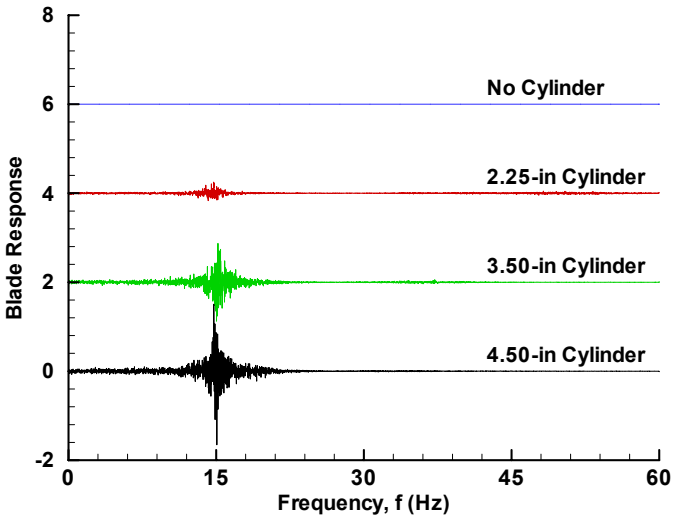

Figure 5.1. Blade Strain: No Mechanical Forcing, Variable D, V_∞ =53 ft/s

Figure 5.1 shows blade-response frequency distribution for the three cylinder forcing cases at V_∞=53 ft/s, with no mechanical forcing input from the mechanical shaker. The curves shown in Figure 5.1 were each measured to have zero mean response relative to frequency but have been vertically shifted for better viewing. For the no cylinder case, at no time were any significant blade vibrations at any frequency detected. This demonstrated that the blade did not have any flutter instabilities induced in the range of velocities investigated. Overall, the freestream itself is not found to induce any significant blade vibrations at any frequency, however, the cylinder-induced forcing produces both a measurable strain and frequency response. The magnitude of this response increases both with increased cylinder size (Figure 5.1) and increased freestream velocity (Figure 5.2).

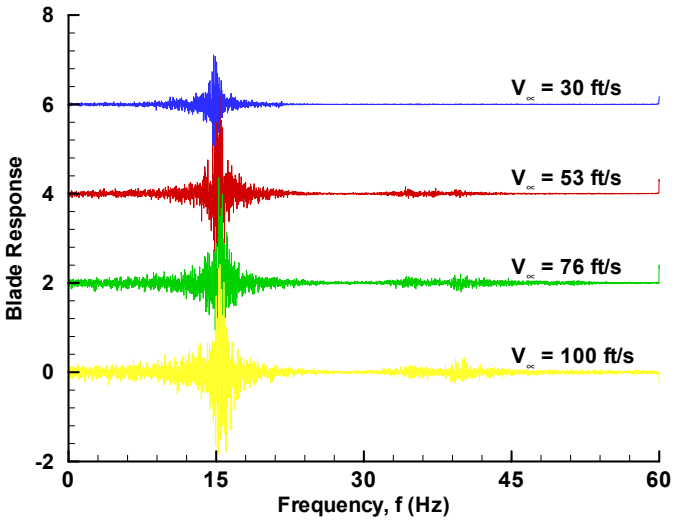

Figure 5.2. Blade Strain: No Mechanical Forcing, Variable V_∞, D=3.50-in.

The frequency response is centered at 15 Hz. The strength increases both with increasing freestream velocity and cylinder diameter.

For each forcing cylinder case, blade strain was measured at multiple frequencies, with the most energy content located near 15 Hz. A 15 Hz response corresponds to the approximate first bending-mode natural frequency of the blade in its current set-up. Given that at V_∞=53 ft/s the expected cylinder induced aerodynamic forcing frequencies were 48, 34 and 26 Hz for the 2.376-in, 3.50-in, and 4.50-in cylinders, respectively, the forcing frequencies were not equal to the natural frequency. This frequency mismatch implies that either the blade aerodynamic damping was reduced by the presence of the propagating cylinder vortical wakes, the wake amplification greatly increased with cylinder diameter, or the wake harmonic content included frequencies near 15 Hz. Figure 5.1 also indicates strain amplification with increasing cylinder diameter at constant freestream velocity, again either corresponding to the lower aerodynamic forcing frequencies, nearer to the blade natural frequency, of wake amplitude differences. Direct measurement of the cylinder induced forcing functions was discussed in chapter 4.

Figure 5.2 illustrates blade-response frequency distribution for the four freestream velocities, with the 3.50-in cylinder and no mechanical forcing. The data in Figure 5.2 similarly indicate response at, or near, the blade natural frequency of 15 Hz, independent of freestream velocity. Increasing velocity does produce marginally greater response amplitude, despite the increase in aerodynamic forcing frequency with velocity (e.g., the 3.50-in cylinder forcing frequency increases from 19 Hz – 65 Hz over the measured velocity range). As will be discussed below, such results suggest forcing-function amplitude increases with freestream velocity.

Corresponding to the data of Figure 5.3 and Figure 5.4, blade-strain probability distributions are presented for each forcing case to illustrate the non-deterministic distribution of blade strain and its dependence on forcing. Figure 5.3 shows blade-strain probability distributions for the three forcing cylinder cases at V_∞ = 53 ft/s, with no mechanical forcing. For the 2.376-in cylinder, Figure 5.3 indicates blade strain to be relatively low with little variability; leading to the large data spike near zero strain. Conversely, blade strain for the 3.50-in and 4.50-in cylinders becomes progressively greater and more variable with increasing diameter (note the × 15 data amplification in Figure 5.3 for illustration). The large-cylinder data also exhibit probability distributions corresponding to a approximately random (bell shaped) strain, even though cylinder wakes are known to produce periodic forcing.[10,11] A probability distribution for a theoretical purely sinusoidal strain with 500 με amplitude is included in Figure 5.3, emphasizing the non-sinusoidal nature of the measured strain distributions. Note the sinusoid distribution is slightly skewed by the strain increment selected in generating the distribution.

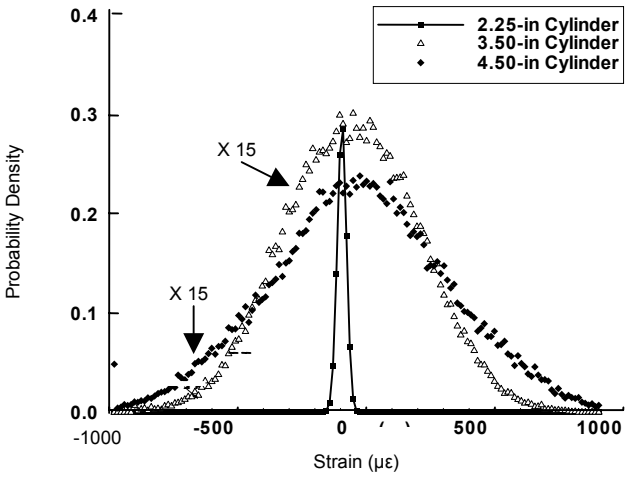

Figure 5.3. Strain Probability: No Mechanical Forcing, V_∞ = 53 ft/s.

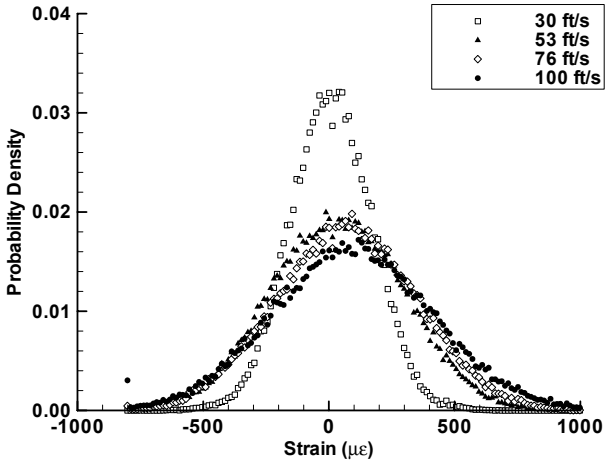

Figure 5.4. Strain Probability: No Mechanical Forcing, D = 3.50-in.

Blade-strain probability distributions for varying freestream velocities, with the 3.50-in cylinder and no mechanical forcing, are shown in Figure 5.4. Clearly, lower freestream velocities produce less strain variability, while progressively higher velocities result in broader distributions. Note that above V_∞ = 53 ft/s the probability distributions are nearly independent of freestream velocity, again showing a bell shaped distribution.

In interpreting the results of Figure 5.3 and Figure 5.4, it should be noted that Sears[13] theoretically predicted aerodynamic loading of a thin flat-plate airfoil due to

sinusoidal forcing (or gusts). He showed airfoil loading to increase with forcing function amplitude and decrease with reduced frequency, as defined by

$$k = \frac{\omega c}{2V_\infty}, \qquad (2)$$

where $\omega = 2\pi f$. Therefore, since reduced frequency decreases with increasing cylinder diameter at constant freestream velocity (i.e., k = 1.47, 0.94, and 0.73, respectively), the strain amplification observed at larger cylinder diameters in Figure 5.3 corresponds with decreased reduced frequency, agreeing with the results of Sears. Conversely, the data in Figure 5.4 were collected at constant reduced frequency (k = 0.94). Thus, the stain augmentation at higher freestream velocities is likely a result of forcing function amplitude, with the V_∞ = 30 ft/s case providing the least forcing. Note that cylinder-shed vortex size and strength is a known non-linear function of freestream velocity.[14] Unfortunately, cylinder-shed vortex characteristics cannot be verified without direct forcing-function measurement, and do not account for the influence of aerodynamic damping. Finally, it is argued that the observed bell shaped strain distributions are a result of either a non-sinusoidal forcing function, multi-modal blade response, or complex fluid-structure interaction; as may be investigated through additional aerodynamic forcing-function and/or blade displacement measurements.

5.2 Sinusoidal Forcing

Sinusoidal mechanical forcing was accomplished at a constant amplitude and frequency (10 Hz). The forcing frequency and amplitude were selected to minimize shaker force input, maximize blade displacement, and reduce the number of excited blade vibration modes. Although the blade first-bending mode was determined to have a

natural frequency near 15 Hz, parametric experimentation showed mechanical forcing above 10 Hz to produce resonant vibrations in the blade supporting structure. Significantly higher frequencies (e.g., above 50 Hz) were also not considered due to shaker limitations. Forcing amplitudes were limited by slot size in the test-section floor (to minimize flow leakage) and the shaker stroke length. The displacement amplitude used for all sinusoidal forcing experiments corresponded to a voltage input of 70mVpp to the shaker.

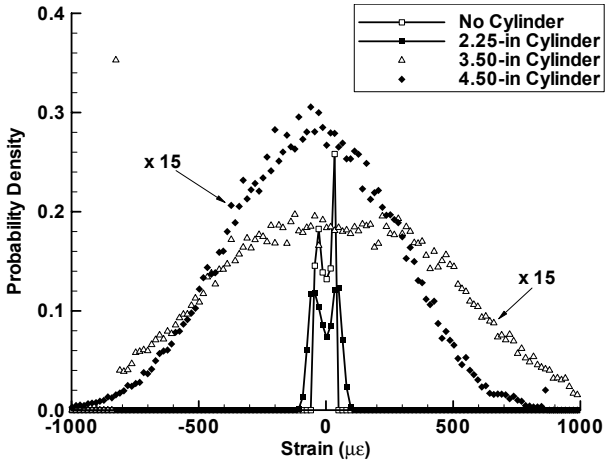

Figure 5.5. Strain Probability: Sinusoidal Forcing, V_∞ = 53 ft/s.

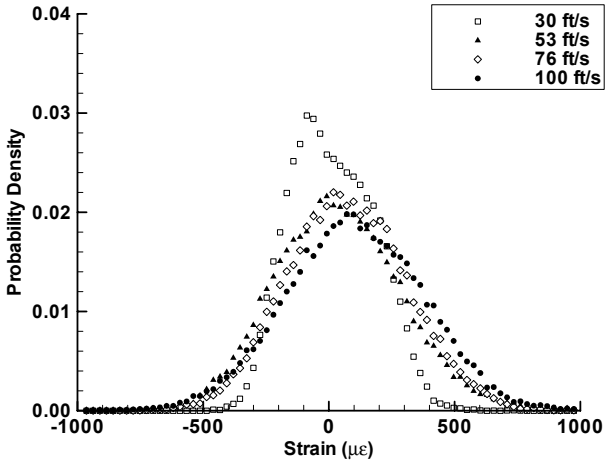

Figure 5.6. Strain Probability: Sinusoidal Forcing, D = 3.50-in.

Blade-strain probability distributions for the three forcing cylinder cases at V_∞ = 53 ft/s, with sinusoidal mechanical forcing, are illustrated in Figure 5.5. With no forcing cylinder, a sinusoidal-like probability distribution is found, as expected for sinusoidal forcing. The asymmetry of the no cylinder distribution is due to the strain increment selection in generating the distribution, and is not an artifact of the measured strain. For the 2.376-in cylinder case, aerodynamic forcing is found to marginally broaden the probability distribution, as expected for the relatively low forcing influence of the 2.376-in cylinder (as suggested by Figure 5.5 and Figure 5.3). Conversely, a drastic departure from the sinusoidal distribution is observed for the 3.50-in and 4.50-in cylinders, indicating a much expanded range of possible blade strains. Note that while the strain increases for the 3.50-in cylinder case, presumably due to a decrease in reduced frequency, some remnants of a sinusoidal-like distribution remain. The 4.50-in cylinder case exhibits no resemblance to a sinusoidal-like distribution, as the aerodynamic forcing clearly dominates the mechanical forcing. Moreover, strain distributions for the larger cylinders are again approximately bell shaped, strengthening the assertion that unsteady aerodynamic interactions more significantly impact blade response than mechanical forcing, at least for the mechanical forcing conditions studied in this investigation. Finally, note that the non-zero mean strain for the 4.50-in cylinder case could be a remnant of the root-mean-square (RMS) strain produced by mechanical forcing, the results of a slight non-zero blade incidence angle relative to the freestream, or most likely an undetected thermal drift in the bridge null strain with time.

The variation in blade-strain probability distribution with freestream velocity, using the 3.50-in cylinder and sinusoidal mechanical forcing, is shown in Figure 5.6. Similar to

the no mechanical forcing case, blade strain distribution is found to broaden with increasing freestream velocity. Higher freestream velocities also causes the strain to depart from a sinusoidal-like distribution, producing a more bell shaped blade response. Again, since the data in Figure 5.6 were collected at constant reduced frequency (k = 0.94), it is argued that the observed distribution differences are a strong function of forcing-function amplitude. In fact, the more sinusoidal-like strain distribution at V_∞ = 30 ft/s is likely due to a decreased-strength wake shed from the upstream cylinder.

5.3 Impulse Forcing

Single-impulse forcing was imparted to the blade via transmission of an isolated mechanical impulse from the shaker. Several different impulse amplitudes and durations were examined in an effort to cause blade resonant vibration. A nominal blade-root-displacement of 0.0315 in (approximately four times that of the sinusoidal mechanical forcing displacement) was necessary to induce a vibration. Larger impulse amplitudes were limited by slot size in the test-section floor. Impulse duration for all experiments was 20 ms; the optimum time determined to produce blade free vibration.

Blade-strain probability distributions for the three forcing cylinder cases at V_∞ = 53 ft/s, with a single mechanical impulse, are illustrated in Figure 5.7. By comparison of Figure 5.7 and Figure 5.3 (no forcing) it is evident that, for the examined forcing amplitude, the impact of a single impulse on blade strain is minimal. However, a slight broadening and mean-shift in the strain distribution for the 4.50-in cylinder case is observed. Such distribution changes for the 4.50-in cylinder may be attributed to possible thermal drift in the bridge null, and/or data repeatability. Data repeatability will be established in follow-

on work,[12] verifying the apparently random blade strain with aerodynamic forcing (particularly with the 3.50-in and 4.50-in cylinders).

Blade-strain probability distribution dependence on freestream velocity, using the 3.50-in cylinder and a single mechanical impulse, is illustrated in Figure 5.8. Again, Figure 5.8 shows little difference from the no mechanical forcing case of Figure 5.4, except at V_∞ = 30 ft/s. Based on previous results, the distribution broadening observed at V_∞ = 30 ft/s is to be expected, given the corresponding reduced influence of aerodynamic forcing. When aerodynamic and mechanical forcing are of similar magnitudes (as is the case at V_∞ = 30 ft/s), an impulse influences blade response over a much longer time period, causing strain deviation from the no forcing case. If, however, aerodynamic forcing dominates the forcing environment, the impact of a single impulse on blade strain is lost.

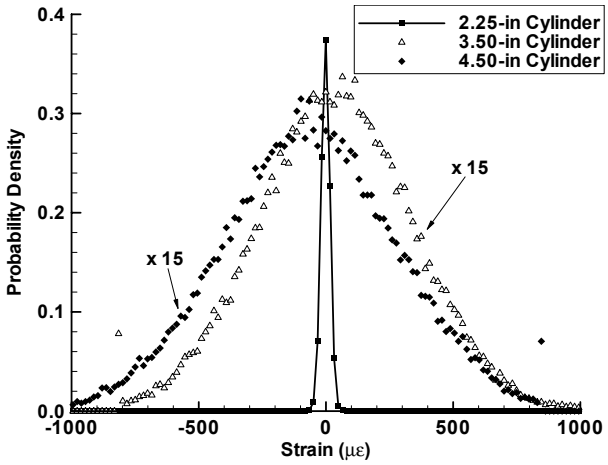

Figure 5.7. Strain Probability: Single Impulse Forcing, V_∞ = 53 ft/s.

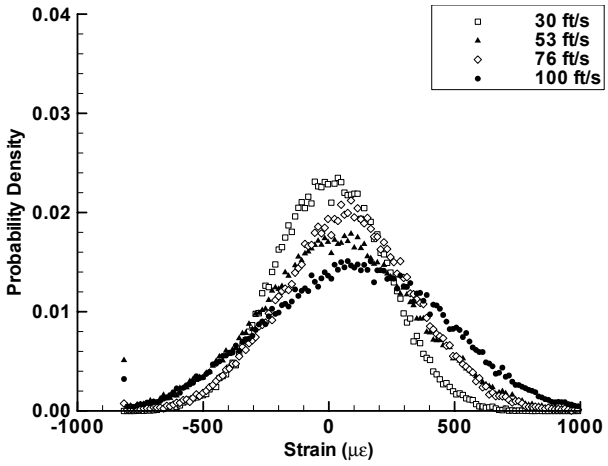

Figure 5.8. Strain Probability: Single Impulse Forcing, D = 3.50-in.

5.4 Sinusoidal and Impulse Forcing

This section will describe the effects of the mechanical forcing on the frequency distributions and the strain probability curves.

5.4.1 Variable-Frequency Multiple Impulses

Multiple-impulse mechanical forcing with variable frequency, but constant amplitude, was imparted to the blade through a series of repeated mechanical impulses from the shaker. Four impulse frequencies were examined, each frequency at a subsequently higher value, corresponding to f_1 = 100 mHz, f_2 = 300 mHz, f_3 = 600 mHz, and f_4 = 1800 mHz, respectively. Time series of blade response for this case, at V_∞ = 53 ft/s with no forcing cylinders, are shown in Figure 5.9. Note the time series in Figure 5.9 were each measured with zero mean response relative to time, but have been vertically shifted for better viewing. Figure 5.9 shows that at the lower frequencies (e.g., at f_1 = 100 mHz), blade transient response to each impulse completely subsides before the subsequent impulse. Conversely, at higher frequencies (e.g., at f_4 = 1800 mHz), blade

transient response to each impulse is interrupted by the following impulse. Response amplitude clearly does not depend on frequency; each impulse induces the same amplitude independent of the previous blade motion. No response amplification is observed when an impulse occurs before the effects of the previous impulse decay.

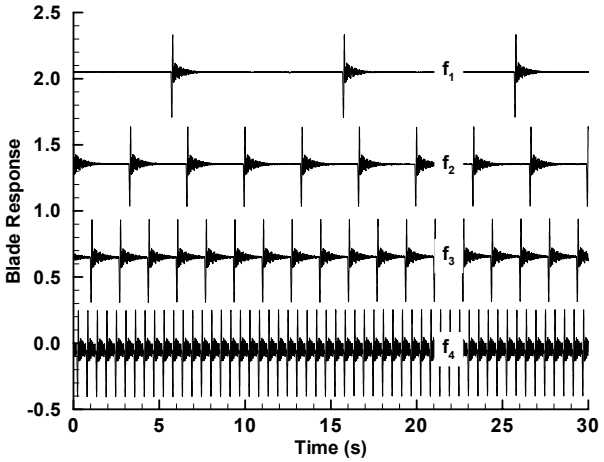

Figure 5.9. Blade Strain: Variable-Frequency Mechanical Impulse,

No Cylinders, $V_\infty = 53$ ft/s.

Corresponding blade-strain probability distributions for the variable-frequency multiple-impulse cases are shown in Figure 5.10. Note that the blade-strain amplitudes are significantly lower than those induced by aerodynamic forcing, particularly compared to the 3.50-in and 4.50-in cylinder cases. Larger amplitude impulse forcing was limited by slot size in the test-section floor. As would be expected based on Figure 5.9, at low impulse frequencies blade strain exhibits a very narrow probability distribution, with little deviation form the mean value; i.e., the likelihood of a large strain is low. At higher frequencies, however, strain distributions are almost flat, suggesting nearly equal probability of occurrence for any measured strain; i.e., the blade spends equally as much time at both high and low strain values. Note that the -50 με mean-shift in the strain

distributions of Figure 5.10 may be attributed to thermal drift in the bridge null, and is not representative of a physically realistic mean strain.

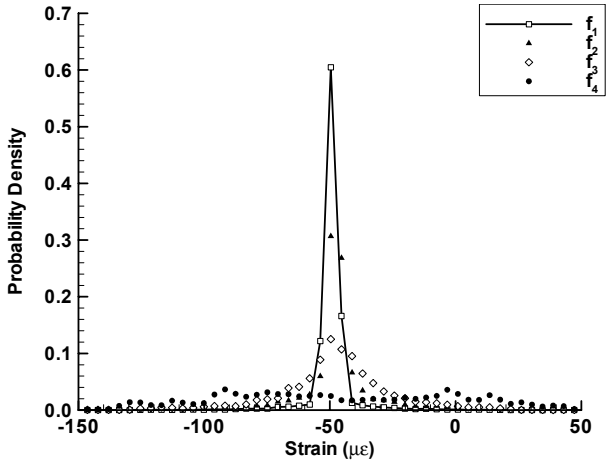

Figure 5.10. Strain Probability: Variable-Frequency Mechanical Impulse, No Cylinders, V_∞ = 53 ft/s.

5.4.2 Variable-Amplitude Multiple Impulses

Multiple-impulse mechanical forcing with variable amplitude, but constant frequency, was imparted to the blade through a series of repeated impulses from the shaker. Three amplitudes were examined, corresponding to A_1 = 90 mVpp, A_2 = 110 mVpp, and A_3 = 140 mVpp input voltage to the shaker, respectively. The lowest impulse amplitude represents the blade minimum displacement producing a measurable free vibration, while the highest amplitude represents the maximum blade displacement given the slot size limitations in the test-section floor. Blade-response time series for this case, at V_∞ = 53 ft/s with no forcing cylinders, are shown in Figure 5.11 with the familiar vertical shifting. Figure 5.11 indicates blade-response amplitude to be relatively unaffected by impulse amplitude, although some slight variation in response duration can be observed. The independence of blade response to impulse amplitude is more likely an artifact of experimental impulse-amplitude limitations, than physical phenomena.

Blade-strain probability distributions for the variable-amplitude multiple-impulse cases are shown in Figure 5.12. Figure 5.12 indicates that, as would be expected, induced blade-strain amplitudes are low. Moreover, the deviation in strain between the different impulse amplitudes is quite small. Note that the mean-shift observed between the three examined forcing amplitudes in Figure 5.12 is on the order of 3.5 με, and therefore within the experimental uncertainty of the measurement instrumentation.

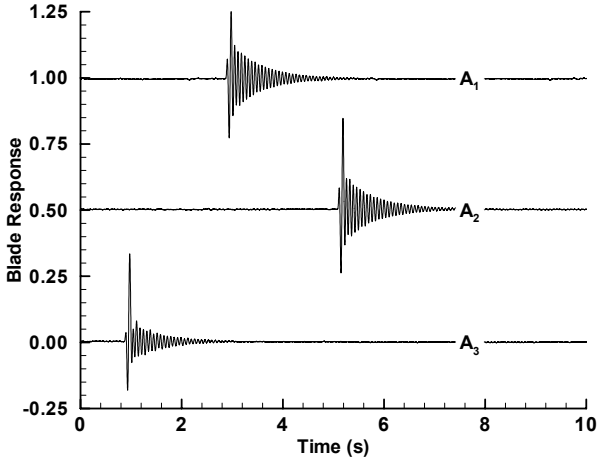

Figure 5.11. Blade Strain: Variable-Amplitude Mechanical Impulse, No Cylinders, V_∞ = 53 ft/s.

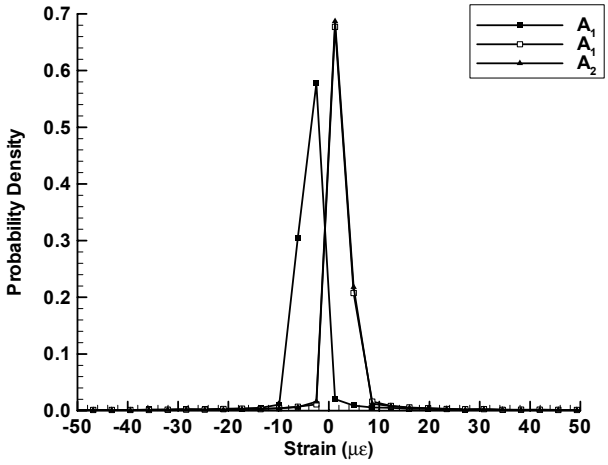

Figure 5.12. Strain Probability: Variable-Amplitude Mechanical Impulse, No Cylinders, V_∞ = 53 ft/s.

No experiments were conducted with aerodynamic forcing and multiple impulses of variable-frequency, or variable-amplitude. However, the expected results from such experiments can be inferred. In particular, multiple high-frequency impulses would likely broaden blade-strain probability distribution in the absence of large aerodynamic forcing, while the effect of multiple variable-amplitude impulses would be minimal (at least for the range of impulse amplitudes investigated).

5.4.3 Random-Amplitude Constant-Frequency Impulses

Multiple-impulse mechanical forcing at constant frequency but random amplitude (aperiodic forcing), was imparted to the blade through a series of mechanical impulses from the shaker. Random amplitude forcing from the shaker was controlled via the programmable waveform generator. Figure 5.13 illustrates time series of blade response for this case at V_∞ = 53 ft/s, with the familiar vertical shifting. Figure 5.13 clearly indicates the relative magnitudes of aerodynamic and mechanical forcing, where by comparing the no-cylinder and 4.50-in cylinder cases it is apparent that aerodynamic forcing dominates mechanical forcing. This is a direct results of cylinder size, cylinder position, freestream velocity, and the limited mechanical forcing amplitude. The non-deterministic nature of blade response in the presence of strong aerodynamic forcing (i.e., in the 3.50-in and 4.50-in cylinder cases) is also indicated by Figure 5.13. As discussed previously, this non-deterministic response is a likely result of non-sinusoidal aerodynamic forcing, multi-modal blade response, or a complex fluid-structure interaction; as could be investigated via additional aerodynamic forcing-function and/or blade displacement measurements. Finally, Figure 5.13 does exhibit some impulse-

induced strain variability for the no-cylinder and 2.376-in cylinder cases, where aerodynamic forcing is reduced.

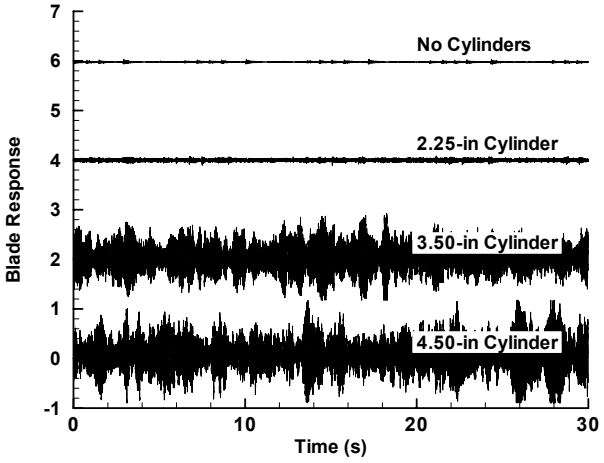

Figure 5.13. Blade Strain: Constant-Frequency Random-Amplitude Mechanical Impulse, $V_\infty = 53$ ft/s.

Blade-strain probability distributions for the constant-frequency random-amplitude impulse forcing are shown in Figure 5.14, at $V_\infty = 53$ ft/s. By comparison between Figure 5.14 and Figure 5.7 (single impulse), it is evident that the multiple-impulse case displays a slightly broader strain probability distribution with the 2.376-in cylinder. Multiple impulses increase the likelihood of larger blade-strain values. For the larger cylinder cases, the effect of multiple impulses is minimal as compared to the single impulse, due to the overpowering influence of the corresponding aerodynamic forcing. Again, any mean-strain distribution shifts may be attributed to possible thermal drift in the bridge null, and/or data repeatability. Similarly, by comparison of Figure 5.15 and Figure 5.8 (single impulse), the constant-frequency random-amplitude impulse forcing is found to have little impact on blade-strain probability distribution at all examined freestream velocities. Once more, this can be attributed to the relatively large influence of the aerodynamic forcing versus the mechanical forcing with the 3.50-in cylinder.

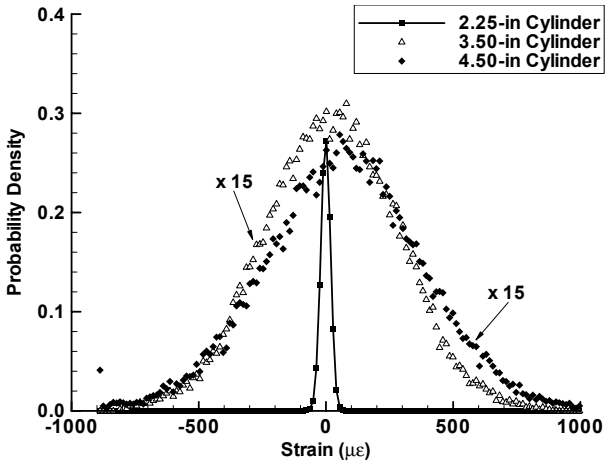

Figure 5.14. Strain Probability: Multiple Random-Amplitude Mechanical Impulse, V_∞ = 53 ft/s.

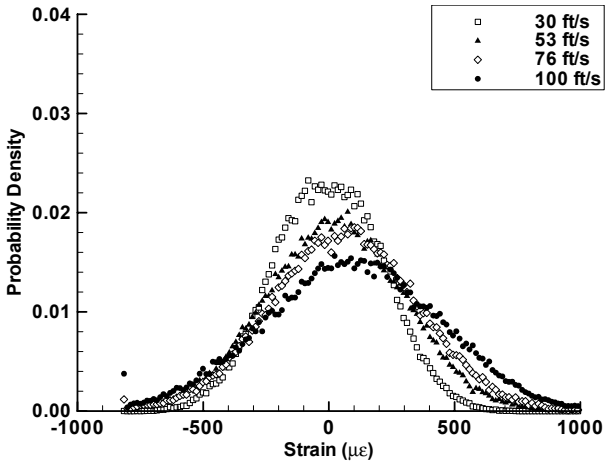

Figure 5.15. Strain Probability: Multiple Random-Amplitude Mechanical Impulse, D = 3.50 in.

5.4.4 Combined Sinusoidal/Impulse Forcing

Ten random-amplitude, constant-frequency impulses, with concurrent sinusoidal mechanical forcing, were imparted to the blade through the shaker. Blade-strain probability distributions for this combined sinusoidal/impulse forcing are shown in Figure 5.16, at V_∞ = 53 ft/s. A direct comparison between Figure 5.16 and the corresponding sinusoidal-forcing data in Figure 5.5 (sinusoidal forcing) shows the

superimposed impulse forcing has two effects. First, any correspondence to a sinusoidal-like probability distribution is removed by the impulses, as would be expected. Second, the blade-strain distribution for each cylinder case is considerably narrower, leading to lower blade-strain values than the corresponding sinusoidal-forcing distributions. This narrowing of the probability distribution contradicts previous data that suggest impulse forcing to broaden blade-strain probability distributions, leading to higher strain values. The cause of this distribution narrowing is unknown at this time, however, several possibilities exist. In particular, due to the function generator characteristics, the construction of a combined sinusoidal/impulse waveform as input to the shaker varied from that of a pure sinusoid. A consistent sinusoid-forcing amplitude was sought between the two experiments, be never verified. In addition, due the large number of forcing cycles measured in this investigation, strain-gage fatigue, and therefore data repeatability, may have been a factor. Data repeatability will be examined in a follow-on investigation using new strain-gage instrumentation.[12]

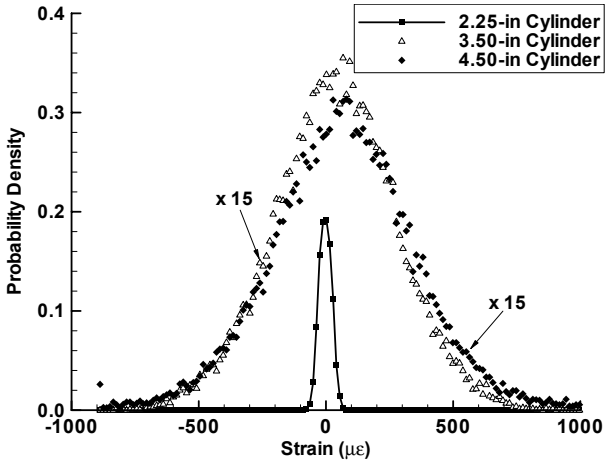

Figure 5.16. Strain Probability: Combined Sinusoidal/Impulse Forcing, V_∞ = 53 ft/s.

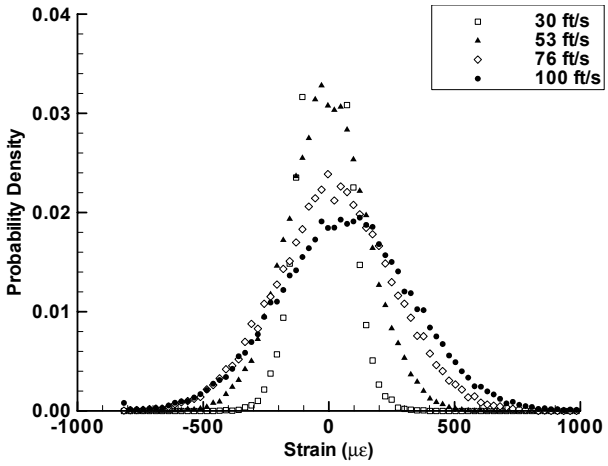

Figure 5.17. Strain Probability: Combined Sinusoidal/Impulse Forcing, D = 3.50 in.

Figure 5.17 shows blade-strain probability distributions for the combined sinusoidal/impulse forcing with the 3.50-in cylinder. Like Figure 5.16, a comparison between Figure 5.17 and Figure 5.6 (sinusoidal forcing) indicates the impact of impulse superposition is primarily to narrow the probability distributions at V_∞ = 30 ft/s and 53 ft/s. Notably, no strain distribution narrowing is observed at the higher freestream velocities (V_∞ = 76 ft/s and 100 ft/s), indicating that the narrowing phenomenon may be physical in nature and not a consequence of the instrumentation, as previously discussed.

6 Conclusions

Results from a series of low-speed wind-tunnel experiments are presented, showing the strain deviation on a single simply-supported blade undergoing various types of both mechanical and aerodynamic forcing. Mechanical forcing types included no forcing, sinusoidal forcing, impulse forcing, and combined sinusoidal-impulse forcing. Impulse mechanical forcing was conducted via single impulse, multiple variable-frequency impulses, multiple variable-amplitude impulses, and multiple random-frequency impulses. Aerodynamic forcing consisted of a von Karman vortex street convecting across the blade from an upstream cylinder.

In general, the influence of impulse mechanical forcing was found to broaden the blade-strain probability distribution to higher strain values, as compared to no forcing or purely sinusoidal mechanical forcing. Furthermore, this broadening influence was found to be highly dependent on the impulse frequency, with a rapid succession of impulses greatly amplifying the possibility of high strain values. For the impulses studied, impulse amplitude or structure (random versus coherent) only slightly influenced strain distribution; however, it can be inferred from the presented results that larger impulse amplitudes than those studied herein would have a significant broadening impact on strain probability distribution.

Aerodynamic forcing greatly influenced blade-strain probability distribution, often overshadowing the mechanical forcing (which was limited by the shaker input

capabilities). For the cylinder cases examined, aerodynamic forcing caused strain distribution to significantly broaden, becoming approximately random in nature. Aerodynamic forcing at low reduced frequency produced greater blade response, while at constant reduced frequency forcing-function amplitude most likely affected blade response.

Overall, results from this investigation confirm the initial premise: the impact of aperiodic (or impulse) forcing on blade response leads greatly increases the probability of higher strain values compared to the periodic forcing case. This is true both with and without aerodynamic forcing. Therefore, the inclusion of probabilistically derived blade-strain histories, which include the influence of blade-resonance events, is likely a necessary step toward reducing the occurrence of HCF failures in turbine engines.

The results of the present investigation clearly indicate the need for further testing to resolve several lingering issues regarding both the mechanical and aerodynamic forcing. Further experiments should include the blade spanwise and chordwise displacement (modal) behavior and the blade aerodynamic damping and expand direct measurements of the cylinder-induced aerodynamic forcing function. Furthermore, other issues such as mean-strain drift, blade flutter and data repeatability should be inverstigated more fully.

Beyond these more basic experiments and analysis, it is clear that an investigation including the influences of blade rotation, neighboring blades, blade-row interactions, and mean aerodynamic loading, as found in an actual rotor, is needed. Such an investigation would confirm the relative impact of impulse forcing on blade-strain

response, and verify the need for continued modeling of aperiodic (probabilistic) blade forcing, forcing functions, and blade-strain distributions.

References

1. Whaley, P. W., 1987, "A Mathematical Model for Internal Friction and Local Fatigue Damage Based on Populations of Yielding Microelements," *ASME Journal of Vibration, Acoustics, Stress, and Reliability in Design*, Vol. 109, pp. 201-206.

2. Whaley, P. W., 1991, "High-temperature Constitutive Theory Based on Populations of Yielding Microelements," Proceedings of the ASME Winter Annual Meeting, Atlanta, GA.

3. Whaley, P. W., 1995, "A New Constitutive Model for Several Metals Under Arbitrary Temperature and Loading Conditions," *ASME Journal of Engineering for Gas Turbines and Power*, Vol. 117, p. 354.

4. Whaley, P. W., 1996, "A Probabilistic Model for Inelastic Deformation," Proceedings of the 1996 ASME International Mechanical Engineering Congress and Exposition, Atlanta, GA.

5. Sanders, A. J., and S. Fleeter, 2002, "Rotor Blade-to-Blade Wake Variability and Effect on Downstream Vane Response," *AIAA Journal of Propulsion and Power*, Vol. 18(2), pp. 456-464.

6. Bisplinghoff, R. L., H. Ashley, and R. L. Halfman, 1955, *Aeroelasticity*, Dover Publications, Inc., Mineola, NY.

7. White, F. M., 1994, *Fluid Mechanics*, Third Edition, McGraw-Hill, Inc., New York, NY.

8. Manwaring, S. R., D. C. Rabe, C. B. Lorence, and A. R. Wadia, 1997, "Inlet Distortion Generated Forced Response of a Low-Aspect-Ratio Transonic Fan," *AIAA Journal of Turbomachinery*, Vol. 119(10), pp. 665-676.

9. Kenyon, J. A., D. C. Rabe, and S. Fleeter, 1999, "Aerodynamic Effects on Blade Vibratory Stress Variations," *AIAA Journal of Propulsion and Power*, Vol. 15(5), pp. 675-680.

10. Fabian, M. K. and Jumper, E. J., 1999, "Rearward Forcing of an Unsteady Compressible Cascade," *AIAA Journal of Propulsion and Power*, Vol. 15(1), pp. 23-30.

11. Fabian, M. K., Falk, E. A., and Jumper, E. J., 2001 "Upstream-Propagating Potential Disturbances Interacting with a Compressible Cascade," *AIAA Journal of Propulsion and Power*, Vol. 17(2), pp. 262-269.

12. Sears, W. R., 1941, "Some Aspects of Non-Stationary Airfoil Theory and Its Practical Application," *Journal of the Aeronautical Society*, Vol. 18, pp. 104-108.

13. Kuethe, A. M. and Chow, C., 1986, *Foundations of Aerodynamics: Bases of Aerodynamic Design*, Fourth Edition, John Wiley & Sons, New York, NY.

14. Jørgensen, F. E., 2002, "How to Measure Turbulence with Hot-Wire Anemometers-A Practical Guide," Dantec Dynamics, Publication no.: 9040U6151, Skovlunde, Denmark.

15. Kline, S. J., 1985 "The Purposes of Uncertainty Analysis", *Journal of Fluids Engineering*, Vol. 107, June 1985, pp. 153-160.

16. Buffum, D. H., and Fleeter, S., 1990, "The Aerodynamics of an Oscillating Cascade in a Compressible Flow Field," *Journal of Turbomachinery,* Vol. 112, October, pp.759-767

17. Crawley, E. F., 1983, "Aerodynamic Damping Measurements in a Transonic Compressor," *Journal of Engineering Power,* Vol. 105, July, pp.575-584

18. Frey, K. K., and Fleeter, S., 2001, "Oscillating Airfoil Aerodynamics of a Rotating Compressor Blade Row," *Journal of Propulsion and Power,* Vol. 17, No.2, March-April, pp. 232-239

19. Kielb, J. J., Abhari, R. S., 2003, "Experimental Study of Aerodynamic and Structural Damping in a Full-Scale Rotating Turbine," *Journal of Engineering for Gas Turbine and Power,* Vol. 125, pp. 102-112

20. Srinivasan, A. V., 1984, "Vibrations of Bladed-Disk Assemblies --- A Selected Survey," *ASME Journal of Vibration, Acoustics, Stress, and Reliability in Design,* Vol. 106, April, pp. 165-168

21. White, F.M., 1991, *Viscous Fluid Flow*, Second Edition, McGraw-Hill, Inc., New York, NY

Appendix A: Uncertainty Analysis

In this appendix the procedure and results for the uncertainty analysis of the anemometer, laser vibrometer, and strain gages will be presented.

A.1 Uncertainty of the Anemometer Velocity

The uncertainty analysis for the anemometer will follow the ISO uncertainty model decribed by Jørgensen[14](2002). An x-wire probe is used. The error of each wire is assumed to be the same because the measurements were taken under identical conditions, the wires were calibrated at the same time, and the wires were manufactured and designed to perform identically.

The first source of uncertainty is from the calibration of the wires. The uncertainty due to the calibration is determined by:

$$U_{cal} = \frac{1}{100} STDV(U_{calibration}(\%)) \qquad \textbf{Equation 2}$$

Here the term $STDV(U_{calibrator}(\%))$ is the calibrator uncertainty, which is 1.6% for the pitot-static tube with calibrated micro-manometer calibration used. This value was obtained using the method of S. J. Kline[15].

The next source of error comes from the curve fitting process and can be calculated from:

$$U_{lin} = \frac{1}{100} STDV(\Delta U_{lin}(\%)) \qquad \textbf{Equation 3}$$

Here the $STDV(\Delta U_{lin}(\%))$ represents the standard deviation of the errors from curve fitting the calibration points.

The DAQ card introduces uncertainty from the input voltage range (E_{AD}), its resolution (n), the velocity of the flow it is measuring (U), and the slope of the inverse calibration curve ($\partial U/\partial E$) found from the derivative of the inverse of the calibration curve. This associated error is found from:

$$U_{res} = \frac{1}{\sqrt{3}} \frac{1}{U} \frac{E_{AD}}{2^n} \frac{\delta U}{\delta E} \qquad \textbf{Equation 4}$$

Probe positioning uncertainty can be affected by the alignment of the probe in the setup of the experiment after calibration. If it is mounted in an orientation different than that of which it was mounted in the calibration an error will be introduced. However, for these experiments the probe was not moved after the calibration was performed so the probe positioning uncertainty does not need to be included.

Temperature variations can cause two sources of uncertainty defined by:

$$U_{temp} = \frac{1}{\sqrt{3}} \frac{1}{U} \frac{1}{T_w - T_0} \left(\frac{A}{B} U^{-0.5} + 1 \right)^{0.5} \qquad \textbf{Equation 5}$$

$$U_{\rho,T} = \frac{1}{\sqrt{3}} \frac{\Delta T}{273} \qquad \textbf{Equation 6}$$

where U is the velocity of the flow, A and B are calibration curve fit constants, T_w is the probe temperature and T_0 is the reference temperature. These two sources are related to the air density and the sensors overheat settings. U_{Temp} represents the error induced by the overheat settings. $U_{\rho T}$ represents the uncertainties related to temperature and density change where only the temperature affects the pressure. The two temperature related uncertainties must be added arithmetically before being combined into the final error calculation.

Ambient pressure variations can also affect the uncertainty in velocity measurements by changing the density of the flow. This change is represented by:

$$U_{\rho P} = \frac{1}{\sqrt{3}} \bullet \left(\frac{P_0}{P_0 + \Delta P} \right)$$ **Equation A.7**

where P_0 is the reference pressure and ΔP is the change in pressure over the span of the measurement. In this experiment the ambient pressure remained constant throught out the experiment, thus will not be included in the uncertainty.

Humidity is the last environmental effect on the uncertainty of a velocity measurement. These changes under normal conditions are negligible and will only come into effect if a change in gas composition is realized during the measurement. In this analysis this has not been the case so this potential source of uncertainty will be disregarded.

To determine the total error of a one wire velocity calculation the errors are combined using the root sum of the squares:

$$U_{wire} = 2 * \sqrt{\Sigma U^2}$$ **Equation 8**

When combining all errors in this manner it is found that there is a 3.7% expected uncertainty in the velocity measurements. The total velocity is defined as:

$$V_{total} = \sqrt{V^2 + U^2}$$ **Equation 9**

where V is the velocity of the first wire and U is the velocity of the second. To find the uncertainty in the total velocity measurement the method of Kline can be employed:

$$U_{total} = \sqrt{\left(U_{wire} \frac{\delta V_{total}}{\delta V} \right)^2 + \left(U_{wire} \frac{\delta V_{total}}{\delta U} \right)^2}$$ **Equation 10**

A.2 Strain Uncertainty

The uncertainty of the strain measurement also follows the method of S. J. Kline[15].

Strain for the half-bridge configuration is defined as:

$$\varepsilon = \frac{-4V_r}{GF\left[(1+\nu)-2V_r(\nu-1)\right]} \quad \textbf{Equation 11}$$

$$V_r = \left(\frac{V_{Signal}}{V_{EX}}\right)_{Strained} - \left(\frac{V_{Signal}}{V_{EX}}\right)_{Umstrained} \quad \textbf{Equation 12}$$

The uncertainty for the strain is

$$\mathrm{E} = \left[\left(\frac{\delta\varepsilon}{\delta GF}GF\right)^2 + \left(\frac{\delta\varepsilon}{\delta V_{SigStr}}V_{SigStr}\right)^2 + \left(\frac{\delta\varepsilon}{\delta V_{EXStr}}V_{EXStr}\right)^2 + \left(\frac{\delta\varepsilon}{\delta V_{SigUns}}V_{SigUns}\right)^2 + \left(\frac{\delta\varepsilon}{\delta V_{EXUns}}V_{EXUns}\right)^2\right]^{1/2} \quad \textbf{Equation 13}$$

Table A-1 shows the values used for the different variables in the strain equation and the error associated with each. The signal voltage varies from a possible value of –10 Volts to +10 Volts.

Table A-1 Variables and Defined Values

Variable	Name	Value
GF	Gage Factor	2.110 ± 0.5%
ν	Poisson's Ratio	0.330
V_{EX}	Excitation Voltage	3.7500V ± 0.0219% ± 5.93mV
V_{Sig} V_{Signal}	Signal Voltage	± 0.0914%

The partial derivates in the strain uncertainty equation represent influence coefficients that are used to determine which variable has the greatest effect on the overall uncertainty. The partial derivative equations are shown below. In this set of equations the strained voltages have the subscript Str and the unstrained voltages have the subscript Uns added to the signal or excitation subscript.

$$\frac{\delta\varepsilon}{\delta GF}GF = \frac{-4\left(\left(\frac{V_{Signal}}{V_{EX}}\right)_{Strained} - \left(\frac{V_{Signal}}{V_{EX}}\right)_{Umstrained}\right)}{GF^2\left[(1+\nu)-2\left(\left(\frac{V_{Signal}}{V_{EX}}\right)_{Strained} - \left(\frac{V_{Signal}}{V_{EX}}\right)_{Umstrained}\right)_r(\nu-1)\right]}$$ **Equation 14**

$$\frac{\delta\varepsilon}{\delta V_{SigStr}} = \frac{-4}{V_{EXStr}GF\left[(1+\nu)-2\left(\frac{V_{SigStr}}{V_{EXStr}} - \frac{V_{SigUns}}{V_{EXUns}}\right)(\nu-1)\right]} + \frac{8\left(-\frac{V_{SigStr}}{V_{EXStr}} + \frac{V_{SigUns}}{V_{EXUns}}\right)(\nu-1)}{V_{EXStr}GF\left[(1+\nu)-2\left(\frac{V_{SigStr}}{V_{EXStr}} - \frac{V_{SigUns}}{V_{EXUns}}\right)(\nu-1)\right]^2}$$ **Equation 15**

$$\frac{\delta\varepsilon}{\delta V_{EXStr}} = \frac{4V_{SigStr}}{V_{EXStr}^2GF\left[(1+\nu)-2\left(\frac{V_{SigStr}}{V_{EXStr}} - \frac{V_{SigUns}}{V_{EXUns}}\right)(\nu-1)\right]} - \frac{8\left(-\frac{V_{SigStr}}{V_{EXStr}} + \frac{V_{SigUns}}{V_{EXUns}}\right)(\nu-1)V_{SisUns}}{V_{EXStr}^2GF\left[(1+\nu)-2\left(\frac{V_{SigStr}}{V_{EXStr}} - \frac{V_{SigUns}}{V_{EXUns}}\right)(\nu-1)\right]^2}$$ **Equation 16**

$$\frac{\delta\varepsilon}{\delta V_{SigUns}} = \frac{4}{V_{EXUns}GF\left[(1+\nu)-2\left(\frac{V_{SigStr}}{V_{EXStr}} - \frac{V_{SigUns}}{V_{EXUns}}\right)(\nu-1)\right]} - \frac{8\left(-\frac{V_{SigStr}}{V_{EXStr}} + \frac{V_{SigUns}}{V_{EXUns}}\right)(\nu-1)}{V_{EXUst}GF\left[(1+\nu)-2\left(\frac{V_{SigStr}}{V_{EXStr}} - \frac{V_{SigUns}}{V_{EXUns}}\right)(\nu-1)\right]^2}$$ **Equation 17**

$$\frac{\delta\varepsilon}{\delta V_{EXUns}} = \frac{-4V_{SigUbs}}{V_{EXUns}^2 GF\left[(1+\nu)-2\left(\frac{V_{SigStr}}{V_{EXStr}}-\frac{V_{SigUns}}{V_{EXUns}}\right)(\nu-1)\right]} + \frac{8\left(-\frac{V_{SigStr}}{V_{EXStr}}+\frac{V_{SigUns}}{V_{EXUns}}\right)(\nu-1)V_{SigUns}}{V_{EXUns}^2 GF\left[(1+\nu)-2\left(\frac{V_{SigStr}}{V_{EXStr}}-\frac{V_{SigUns}}{V_{EXUns}}\right)(\nu-1)\right]^2} \quad \textbf{Equation 18}$$

Using the values from Table A-1 and the known recorded values of the strain representational values for V_{Signal} were used to determine the greatest influence coefficient. The gage factor had the greatest effect followed by the unstrained voltage. The largest uncertainty for the strain was $\pm 2.628*10^{-3}\mu\varepsilon$.

A.3 Displacement Uncertainty

The uncertainty for the displacement measurements follows the method S. J. Kline. Displacement is found from the integration of the velocity. Therefore, the uncertainty of the velocity will be found first and then used to find the displacement uncertainty using Simpson's 1/3 integration.

The velocity is found through a simple linear relationship between the voltage and the velocity decoder range scale factor (Equation 19).

$$Velocity = Voltage*125 \qquad \text{Equation 19}$$

The defined linear uncertainty for the laser vibrometer is 1% of full scale. The total calibration uncertainty is 3% (u_{LV}), which includes the linear uncertainty, and the

uncertainty due to the data acquisition card (u_{DAQ}) is 0.0914 % of the reading. Equation 20 shows the uncertainty in the velocity.

$$u_{vel} = \sqrt{\left(\frac{\delta \ln Velocity}{\delta \ln Voltage_{DAQ}} u_{DAQ}\right)^2 + \left(\frac{\delta \ln Velocity}{\delta \ln Voltage_{LV}} u_{LV}\right)^2} \qquad \textbf{Equation 20}$$

Due to the linear nature of the velocity equation both influence coefficients go to 1. Inserting the uncertainty values makes u_{vel} = 3.0014%.

The uncertainty for the displacement is dependent on the method of integration used. Simpson's 1/3 rule was chosen for this analysis, Equation 21.

$$Dis = \frac{1}{3}\left(Vel_1 + 2Vel_2 + Vel_3\right) \qquad \textbf{Equation 21}$$

The uncertainty is then defined as

$$u_{Dis} = \sqrt{\left(\frac{Vel_1}{Dis}\frac{\delta Dis}{\delta Vel_1} u_{Vel_1}\right)^2 + \left(\frac{Vel_2}{Dis}\frac{\delta Dis}{\delta Vel_2} u_{Vel_{21}}\right)^2 + \left(\frac{Vel_3}{Dis}\frac{\delta Dis}{\delta Vel_3} u_{Vel_3}\right)^2} \qquad \textbf{Equation 22}$$

Through simplification and reduction

$$u_{Dis} = \frac{\sqrt{Vel_1^2 + 4Vel_2^2 + Vel_3^2}}{Vel_1 + 2Vel_2 + Vel_3} u_{vel} \qquad \textbf{Equation 23}$$

The absolute value of the coefficient of u_{vel} will always be less than 1. Therefore, the uncertainty for the displacement will be less than the uncertainty for the velocity.

VITA

Trina Sue Krausse

Candidate for the Degree of

Master of Science

Thesis: STUDY OF IMPULSE FORCING ON A SIMPLY SUPPORTED BLADE

Major Field: Mechanical Engineering

Biographical:

Education: Received a Bachelor of Science in Aerospace Engineering from Oklahoma State University, Stillwater, Oklahoma, in December 2002. Completed the Requirements for the Master of Science in Mechanical Engineering degree at Oklahoma State University in May 2005.

Experience: Employed by the Department of Mechanical and Aerospace Engineering, at Oklahoma State University, as a research assistant spring 2003 to spring 2004, also as a teaching assistant for the spring and fall 2004. Also employed by the Mathematics Department, at Oklahoma State University, as a grader from fall 1999 to fall 2004 and as a student financial assistant, May to December 2002.

Professional Memberships: American Institute of Aeronautics and Astronautics, Sigma Gamma Tau (National Honor Society of Aerospace Engineering), Pi Tau Sigma National (Mechanical Engineering Honor Society)

Name: Trina Sue Krausse Date of Degree: May, 2005

Institution: Oklahoma State University Location: Stillwater, Oklahoma

Title of Study: STUDY OF IMPULSE FORCING ON A SIMPLY SUPPORTED BLADE

Pages in Study: 54 Candidate for the Degree of Mater of Science

Major Field: Mechanical Engineering

Results from a series of low-speed wind-tunnel experiments are presented showing the influence of aperiodic forcing on the vibratory and strain response of a simply supported blade. Blade forcing was accomplished via both mechanical and aerodynamic means. Variable amplitude/frequency mechanical forcing was achieved through an electromagnetic shaker, while aerodynamic forcing corresponded to wake shedding from an upstream cylinder. Measured blade-strain probability distributions are presented illustrating the parametric dependencies of blade-strain on freestream velocity, forcing frequency, and forcing amplitude whether the forcing is mechanical, aerodynamic, a combination. These distributions suggest impulse forcing broadens blade-strain probability distributions, producing higher strain values. Impulse forcing frequency significantly impacted blade-strain distribution, while impulse amplitude and coherence were not nearly as influential. Aerodynamic forcing dominated the effects of the examined mechanical forcing, promoting a randomly distributed blade strain about its mean, approximately equal to a bell shaped strain response.

Advisor's Approval: A.S. Arena